J. Fluid Mech. (1992), *vol.* 240, *pp.* 289–313
Printed in Great Britain

Linear-eddy modelling of turbulent transport. Part 7. Finite-rate chemistry and multi-stream mixing

By ALAN R. KERSTEIN
Combustion Research Facility, Sandia National Laboratories, Livermore, CA 94551-0969, USA

(Received 18 July 1991)

The linear-eddy turbulent mixing model, formulated to capture the distinct influences of turbulent convection and molecular transport on turbulent mixing of diffusive scalars, is applied to two mixing configurations in homogeneous flow: a scalar mixing layer and a two-line-source configuration. Finite-rate second-order chemical reactions are considered, as well as the limits of fast reaction and frozen flow. Computed results are compared to measurements in a reacting-scalar mixing layer and in a two-line-source configuration involving passive-scalar mixing. For each configuration, the adjustment of a single model parameter related to the turbulence integral scale yields computed results in good agreement with a variety of measured quantities. The results are interpreted with reference to a simpler model, based solely on large-scale flapping effects, that reproduces many qualitative trends. For three-stream mixing with finite-rate chemistry, a novel dependence of the reactant correlation coefficient on the chemical reaction rate is predicted.

1. Introduction

The linear-eddy modelling approach (Kerstein 1988, 1989, 1990, 1991*a*, *b*, 1992) was introduced in order to capture the principal mechanisms governing the turbulent mixing of diffusive scalars in a physically sound though approximate manner. The governing mechanisms, turbulent convection and molecular transport, are quite dissimilar in their influence on the mixing process. Convection rearranges the spatial location of fluid elements without changing their chemical composition. The chemical composition of a fluid element evolves by molecular transport (i.e. species exchange with neighbouring fluid elements) and by other molecular processes such as chemical reaction.

To date, modelling approaches that lack full spatial resolution have not demonstrably captured these distinct influences in a robust, computationally affordable manner. Such models typically subsume all unresolved fine-scale mechanisms in a mixing submodel that does not preserve the aforementioned mechanistic distinction. This renders the treatment of Schmidt-number (*Sc*) and related effects problematic, as discussed previously (Kerstein 1989, 1990).

Direct numerical simulation based on the three-dimensional Navier–Stokes and species transport equations overcomes this difficulty, but at a cost that is prohibitive for all but the simplest turbulent mixing configurations. The range of accessible problems has been increased by maintaining full spatial resolution but reducing the dimensionality, based on a dynamical equation such as the Biot–Savart vortex interaction law employed in the two-dimensional discrete-vortex method (Leonard 1980). Though not an exact representation of three-dimensional Navier–Stokes

dynamics, such an approach can often capture the essential features of turbulent mixing in configurations of interest (Ghoniem, Heidarinejad & Krishnan 1989).

The linear-eddy approach carries this strategy one step further by invoking a one-dimensional representation of the kinematics of turbulent convection. It is a kinematical rather than a dynamical approach because the convection process is represented by a postulated random process embodying inertial-range scalings rather than by a dynamical equation. The postulated random process, formulated in detail elsewhere (Kerstein 1991*b*), is briefly summarized in §2. In that reference, the approach is validated by means of comparisons to measurements of computed scalar power spectra, higher-order intermittency statistics, and other scalar fluctuation properties. The approach is shown to reproduce many microstructural properties of turbulent mixing fields such as scaling exponents governing power spectra and other multi-point statistics.

This validation does not ensure that the model can reproduce concentration statistics for spatially resolved species in flows with spatially varying mean concentrations due to, e.g. spatially inhomogeneous inlet concentration profiles or chemical reactions. In particular, for the case of turbulent plug flow with specified species concentration profiles in the inlet plane (transverse to the mean flow), one would ideally seek a formulation that could predict the species concentration statistics at any point downstream based on inlet conditions, physicochemical properties (kinematic viscosity ν, species molecular diffusivities, reaction rates, etc.), and a gross characterization of the flow, namely mean velocity U, turbulence integral scale l, and turbulence Reynolds number Re (not necessarily the same as the nominal Reynolds number Ul/ν). One could also seek to predict multi-point concentration statistics. The linear-eddy approach has this capability, as noted earlier, but data comparisons considered here are limited to single-point statistics.

Expressing streamwise development of the mixing field as time evolution based on $x = Ut$, the chemically reacting turbulent plug flow may be viewed as an initial-value problem or, more generally, as an initial-boundary-value problem if flow in a duct of finite cross-section is considered. The formulation of a turbulent mixing model that addresses this problem in its full generality, irrespective of the reliability of its predictions, is in itself challenging. Existing models typically cannot accommodate arbitrary inlet concentration profiles. For instance, particular models may address only two-stream mixing (i.e. all points on the inlet plane constrained to one of two chemical compositions) or only mixing of localized sources imbedded in a compositionally uniform background. For the special case of two-stream mixing of reacting species in turbulent plug flows with negligible transverse variation of mean concentration, simple zero-dimensional models successfully predict the dependence of product formation rates on stoichiometry and related parameters (Mao & Toor 1971; Li & Toor 1986).

A linear-eddy formulation is outlined in §2 that is applicable to homogeneous turbulence with any inlet concentration profile and that depends on only one transverse coordinate. Some relaxation of these constraints is feasible, as demonstrated previously (Kerstein 1989, 1990). The model accommodates multiple species with different molecular diffusivities and finite-rate chemical reactions among the species. The model is applied to two configurations for which available experimental results allow detailed comparisons. For each configuration, the adjustment of a single model parameter related to the turbulence integral scale is found to yield computed results in good agreement with a variety of measured quantities. The results are interpreted with reference to a simpler model that is based

solely on large-scale flapping effects. That 'flapping model' reproduces some but not all measured trends, thus indicating which mixing phenomena are sensitive to the additional mechanisms incorporated in the linear-eddy formulation.

The computed results lead to a novel prediction, namely that the concentration correlation coefficient of two inlet species may be a non-monotonic function of the chemical reaction rate in a multi-stream mixing configuration. Suggestions are offered concerning additional measurements that would check the robustness of the model and provide further insight into turbulent mixing phenomena.

2. Model formulation

Linear-eddy modelling involves the Monte Carlo simulation of the time evolution of the scalar fields $c_j(y,t)$, indexed by species label j, on a one-dimensional domain from given initial conditions $c_j(y,0)$. The simulated evolution is governed by two processes, implemented concurrently, representing molecular and convective effects respectively. In the present formulation, the computational domain represents a transverse line initially in the inlet plane of a turbulent plug flow, convected downstream with the mean flow velocity U. Time evolution of simulated realizations is interpreted as development of the mixing field along the streamwise coordinate x based on the relation $x = Ut$. Spatially resolved fluctuation statistics are developed by computing multiple realizations, yielding one scalar composition per realization at each (x,y) location. Results reported here are typically based on 1000 realizations, giving a coefficient of variation of roughly $1000^{-\frac{1}{2}} \approx 3\,\%$ for estimated quantities (or more for quantities such as higher moments that are especially sensitive to occasional large deviations from typical behaviour).

Since transverse spatial structure of the mixing field is captured only in one direction, denoted y, applications are limited here to planar mixing fields, i.e. to mixing fields whose statistical properties are independent of the orthogonal Cartesian coordinate z. The modelling approach can also accommodate axisymmetric flows, as demonstrated elsewhere (Kerstein 1990). It is recognized that the instantaneous mixing field is nevertheless three-dimensional. The modelling challenge is to capture as much three-dimensional mixing phenomenology as possible in a one-dimensional formulation. Model representations of molecular and convective effects are considered in turn.

Molecular effects are implemented deterministically based on numerical solution of the appropriate governing equations. The governing equations adopted in the present formulation are

$$\partial c_j/\partial t = D_j \nabla^2 c_j + w(c_1,\ldots,c_n), \quad j = 1,\ldots,n \tag{1}$$

where D_j is the molecular diffusivity of species j and the reaction-rate term w is a specified function of the n scalars $c_1,\ldots,c_n$. The scalars may represent species concentrations, temperature, or any other physicochemical property of the fluid. For instance, density variations can be incorporated, though in a somewhat *ad hoc* manner, as shown elsewhere (Kerstein 1992). In applications considered here, c_j represents either a passive, diffusive scalar or a chemically reacting species. Fickian diffusion is adopted, although the modelling approach readily accommodates more general multicomponent diffusion. For clarity, the subsequent discussion is limited to the case of a single scalar, so the subscript on c is dropped and the molecular diffusivity is denoted D_{M}.

Convective effects are represented by a stochastic process consisting of a random

sequence of instantaneous 'rearrangement events' that punctuate the ongoing deterministic solution of (1). These events are the model analogues of inertial-range eddies. Each event is a measure-preserving map of a randomly chosen segment of the computational domain onto itself. In other words, the extent of the spatial domain over which the concentration of any species falls within the range $(c, c+\mathrm{d}c)$ is unchanged by the map. (Recall that the density is taken to be constant.) The measure-preserving property assures that convection rearranges the spatial locations of fluid elements without changing their internal compositions.

The measure-preserving property severely constrains the mathematical specification of individual mapping events. Two alternative specifications have been employed in previous work. Of the two, the 'triplet map' and its generalization to higher 'tuplets' has been shown to provide the better mechanistic representation of the effect of an individual eddy on a scalar field.

The triplet map, adopted here, is conveniently defined as a two-step process. First, the scalar field within the chosen segment is replaced by three compressed copies of the original scalar field within the segment. Each copy is compressed spatially by a factor of three so that the three copies fill the original segment. Second, the middle copy is spatially inverted. Graphical illustrations and a formal mathematical definition of this map, as well as a mechanistic rationale for this formulation, have been presented in Kerstein (1991*a*, *b*).

Rearrangement events are taken to be statistically independent with respect to segment location and time of occurrence. Flow-field inhomogeneity with respect to the y-coordinate can be represented by allowing the mean event frequency and other parameters (specified shortly) that govern the random process to vary with location y along the computational domain. Likewise, flow-field inhomogeneity with respect to the streamwise coordinate x can be represented by allowing the governing parameters to vary with computational time t in accordance with the aforementioned relation $x = Ut$. For present purposes, the flow field is treated as homogeneous with respect to all spatial coordinates. The rationale for this assumption is discussed with reference to specific experimental configurations.

The mean event frequency is characterized by a parameter λ, with units $(\text{length} \times \text{time})^{-1}$, such that the frequency of occurrence of events with segment centres in any interval $[y, y+\Delta]$ is $\lambda\Delta$. The size s of a given segment is randomly selected according to a segment-size probability density function (p.d.f.) $f(s)$. The analogy between rearrangement events and inertial-range eddies motivates the specification of $f(s)$ and the event-frequency parameter λ.

That analogy, developed in detail elsewhere (Kerstein 1991*b*), is based on the observation that the random sequence of maps induces a random walk of each fluid element. The associated diffusivity,

$$D_{\mathrm{T}} = \tfrac{2}{27}\lambda \int_0^\infty s^3 f(s)\,\mathrm{d}s,$$

is the model analogue of the turbulent diffusivity and the ratio $Pe \equiv D_{\mathrm{T}}/D_{\mathrm{M}}$ is the model Péclet number. In applications considered here, Pe is set equal to its measured value for purposes of data comparison, thereby determining λ for given $f(s)$.

To specify $f(s)$, the model incorporates a scaling property based on the Kolmogorov cascade picture of inertial-range turbulence: namely, the diffusivity induced by inertial-range eddies of size s or less is proportional to $s^{\frac{4}{3}}$. (Other values of the exponent have been used in previous work for purposes of sensitivity analysis.) The model analogue of the inertial range is the range $L_{\mathrm{K}} < s < L$ of allowed segment sizes,

where L_K and L are the model analogues of the Kolmogorov scale and the integral scale, respectively. Within this range, $f(s)$ is chosen so that D_T scales as $s^{\frac{4}{3}}$ for $L_K \ll s < L$. Outside the allowed range, $f(s)$ is set equal to zero. These requirements, in conjunction with normalization of the p.d.f., give $f(s) = \frac{5}{3}s^{-\frac{8}{3}}/(L_K^{-\frac{5}{3}} - L^{-\frac{5}{3}})$ for $L_K < s < L$.

The lower bound on the range of segment sizes does not preclude the development of scalar fluctuations at arbitrarily small lengthscales because each mapping event, however large the chosen segment, induces a three-fold compression of the scalar field within the segment. The sequence of mapping events during a realization induces lengthscale compression at an exponential rate. As in real flows, the scalar microscale in simulated realizations is governed by the overall balance between this convectively induced lengthscale compression and the smoothing effect of molecular diffusion. The fidelity of the model representation of these competing mechanisms is indicated by the good agreement with measured scalar spectral properties over a wide range of Sc (Kerstein 1991*b*).

It is convenient to reparametrize the model in terms of the model analogues $Re_S = (L/L_K)^{\frac{4}{3}}$ and $Sc_S = (D_T/D_M)/Re_S = Pe/Re_S$ of the respective physical quantities Re and Sc. The aforementioned comparison of computed and measured spectral properties yielded the empirical relation $Sc_S = 0.51Sc$, which is adopted here. Given the physical quantities Pe and Sc, the ratio L/L_K is determined through the relationships involving Re_S.

With the non-dimensional parameters of the model thus specified in terms of physical quantities, the connection to experimental configurations is completed by specifying two parameters involving length and time. Convenient choices are the molecular diffusivity D_M and the model integral scale L. The definition of L is not equivalent to the operational definition of the measured integral scale l. Therefore L is treated here as an adjustable parameter, chosen for each configuration so that the computed root-mean-square (r.m.s.) fluctuation c' of a passive scalar c matches centreline measurements.

Returning now to the more general case of multiple species undergoing finite-rate chemical reactions, the reaction-rate term in (1) and the molecular diffusivity D_j of each species must now be specified. (Sc_j is assumed proportional to D_j, so all the D_j, and Sc for one species, must be specified.) Applications considered here involve two reactants, labelled A and B, undergoing bimolecular reaction governed by

$$w = -kc_A c_B. \tag{2}$$

For each application, the rate constant k is appropriately scaled to form a Damköhler number Da.

The reported results are based on computations in which the spatial and temporal resolution are sufficient so that finite-sample variability (typically of order 3%, as noted earlier) rather than discretization error was the principal error source. Adequacy of resolution is verified by computing selected cases at higher resolution. For the statistical quantities considered here, there are instances in which resolution much coarser than L_K is adequate, and instances in which resolution much finer than L_K is needed. As in laboratory experiments, computational resolution requirements depend strongly on the quantity being computed, as well as on flow conditions. For the configurations considered here, the typical run time per computed realization is one minute on a Cray XMP-24.

The experiments being simulated were performed in ducted flows, but measurements were reported only for locations not subject to wall effects. Each

simulation is implemented on a finite y-interval with no-flux boundary conditions, and only maps whose segments are entirely contained within the domain are implemented. Consistent with measurement conditions, the domain is chosen to be large enough in each case that the reported results are not subject to boundary effects. Periodic boundary conditions like those adopted in previous applications (Kerstein 1991*b*) would therefore be equally suitable.

In the flows considered here, temperature and pressure variations were small enough that density fluctuations could be neglected. Combusting flows in which thermal expansion influences the flow are addressed elsewhere using a model formulation that incorporates this effect (Kerstein 1992).

3. A scalar mixing layer with finite-rate chemistry

A turbulent reacting flow configuration that provides a useful characterization of chemical-kinetic effects is the reactive scalar mixing layer studied by Bilger, Saetran & Krishnamoorthy (1991). Those investigators measured simultaneously the concentrations of the reactants nitric oxide (NO) and ozone (O_3) at various locations downstream of a turbulence-generating grid, with the respective reactants (diluted with air) introduced on either side of a splitter plate immediately upstream of the grid. The flow conditions, inlet concentrations, and physicochemical properties for the cases considered here are shown in table 1.

NO and O_3 undergo an exothermic bimolecular chemical reaction, forming NO_2 and O_2. At the concentrations indicated in table 1, the resultant temperature rise is small enough that it has negligible effect on the reaction rate or the flow field. The reactant molecular diffusivities are close enough to each other that the concentration difference $[NO]-[O_3]$ is to a good approximation a conserved scalar, as confirmed by the measurements of Bilger *et al.* (1991). (Conserved-scalar analysis is presented in detail in that reference. Following their reference, the reactants NO and O_3 are alternatively denoted A and B, respectively.) Thus, the concentration measurements yield the mixing statistics of a conserved scalar as well as those of reactive scalars for several Da values. Bilger *et al.*'s definition of Da is adopted here, namely $Da = kM\,(c_{A_i}+c_{B_i})/U$, where k is the bimolecular rate constant appearing in (2), M is the mesh spacing of the grid, and the subscript i denotes an inlet condition.

The transverse coordinate y is referenced to the splitter plate. Positive-y and negative-y portions of the inlet plane (taken to be the plane of the turbulence-generating grid) correspond to feed streams containing reactants A and B respectively, with respective inlet-plane concentrations c_{A_i} and c_{B_i}. In terms of these quantities, Bilger *et al.* reported measured fluctuation statistics of the normalized reactive scalars c_A/c_{A_i} and c_B/c_{B_i} and of mixture fraction, a normalized conserved scalar defined as $c = (c_A - c_B + c_{B_i})/(c_{A_i}+c_{B_i})$.

Measurements were performed at two streamwise locations. The data comparisons shown here correspond to the location farther downstream, a distance $x/M = 21$ from the grid. This is not far enough downstream for relaxation of near-field effects of the grid and the splitter plate. Evidence of such effects in the experimental data is noted shortly. Nevertheless, useful data comparisons are possible, reflecting experimental design tradeoffs intended to optimize the characterization of finite-Da effects in a turbulent mixing process.

In the simulations, k and fluid properties are assigned the values shown in table 1, based on values adopted by Bilger *et al.* in their data analysis. Additional simulations are performed with the molecular diffusivities of both reactive scalars set to 0.2 cm^2/s

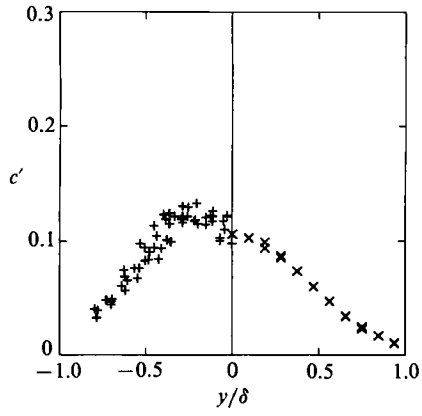

FIGURE 1. Measured (+) and simulated (×) transverse profiles of the r.m.s. fluctuation c' of mixture fraction in the scalar mixing layer at $x/M = 21$. (M is the mesh spacing of the turbulence-generating grid.) Owing to symmetry about the centreline (vertical line), measured (Bilger *et al.* 1991) and simulated profiles are plotted with respect to $-|y|$ and $|y|$, respectively. The transverse location y is scaled by the local width δ of the mean profile $\langle c(y)\rangle$, defined as the y-interval from $\langle c\rangle = 0.1$ to 0.9.

	Configuration	
	Mixing layer	Line source(s)
Molecular properties		
D_M of conserved scalar ($cm^2\ s^{-1}$)	0.20	0.20
D_M of reactant A ($cm^2\ s^{-1}$)	0.18	0.20
D_M of reactant B ($cm^2\ s^{-1}$)	0.22	0.20
Sc of conserved scalar	0.75	0.75
rate coefficient k ($ppm^{-1}\ s^{-1}$)	0.39	n.a.
Reactant concentration (p.p.m.) (two cases, Da in parentheses):	0.7 (0.3) 4.0 (1.8)	n.a.
Flow properties		
grid mesh spacing M (cm)	32	2.5
mean flow velocity U ($cm\ s^{-1}$)	55	700
turbulent diffusivity D_T ($cm^2\ s^{-1}$)	150	8.89
turbulence integral scale l (cm) at indicated distance from grid (in parentheses), in units of M	26 (21)	1.02 (20) 1.35 (52)

TABLE 1. Characteristics of the experimental configurations considered here, the scalar mixing layer of Bilger *et al.* (1991) and the continuous-line-source configuration of Warhaft (1984). The concentrations of reactants A and B (nitric oxide and ozone, respectively) are equal for each indicated case. The turbulent diffusivity is deduced from measurements, as discussed in the text. Molecular properties are based on a nominal temperature of 25 °C.

to assess the importance of differential molecular diffusion of the reactants. Consistent with experimental inference, the effect is found to be negligible in all instances, so the equal-diffusivity results are not reported here. In addition to the reactive scalars, a conserved scalar with molecular diffusivity 0.2 cm^2/s and with the same inlet profile as species A is simulated. The model parameter Sc_S is determined

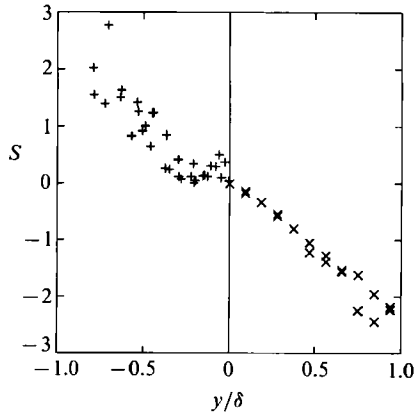

FIGURE 2. Measured (+) and simulated (×) transverse profiles of mixture-fraction skewness S in the scalar mixing layer at $x/M = 21$. Format and definitions as in figure 1, except that points whose y signs are changed also have their S signs changed because S is an odd function of y.

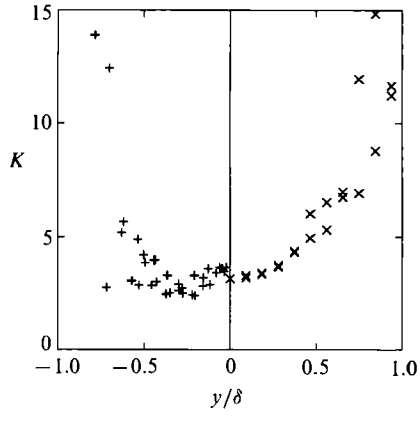

FIGURE 3. Measured (+) and simulated (×) transverse profiles of mixture-fraction kurtosis K in the scalar mixing layer at $x/M = 21$. Format and definitions as in figure 1.

by adopting the empirical relation $Sc_S = 0.51Sc$ (see §2). As noted in §2, empirical determination of the two configuration-specific model parameters D_T and L is also required.

D_T is deduced from the measured spread of the mean mixture-fraction profile $\langle c(y)\rangle$ at $x/M = 21$. The measured profile approximates the error-function form predicted by turbulent-diffusion theory (Libby 1975) and confirmed by previous measurements (LaRue & Libby 1981; Ma & Warhaft 1986). The transverse spread of the profile, characterized by its variance σ^2, determines D_T according to the relation $\sigma^2 = 2D_T t = 2D_T x/U$ governing a Fickian diffusion process with constant D_T. The value $D_T = 150$ cm^2/s is thus obtained.

In fact, other measured properties indicate that D_T varies strongly with x and that it is higher than found previously (LaRue & Libby 1981; Ma & Warhaft 1986), perhaps reflecting the influence of the splitter plate or other near-field effects. These complications could only be addressed computationally by a multidimensional numerical model that simulated the flow field, as well as the scalar mixing field, in

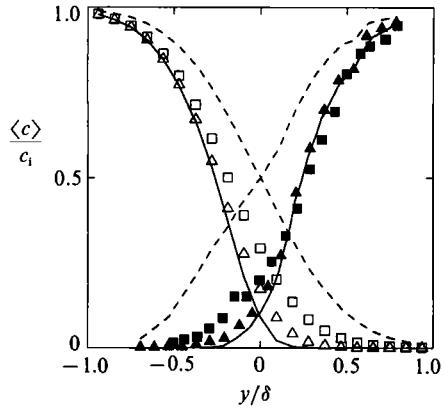

FIGURE 4. Transverse profiles of mean concentration $\langle c \rangle$, scaled by inlet concentration c_i, in the scalar mixing layer at $x/M = 21$ for $Da = 0.3$ (□), 1.8 (△), ∞ (——) and 0 (– – –). Filled symbols: measured NO profiles (Bilger *et al.* 1991). Open symbols; simulated O_3 profiles. Fast-chemistry and frozen-flow profiles for NO are based on conserved-scalar measurements; those for O_3 are based on conserved-scalar simulations.

detail. The simplifying assumption adopted here assures agreement of the simulated mean mixture-fraction profile with the measured profile at $x/M = 21$, but the kinematical process by which that final state is reached is not emulated with quantitative precision. The quantitative impact of this simplification will be discussed.

As mentioned in §2, the parameter L is adjusted so that the centreline value of c', the r.m.s. fluctuation of mixture fraction, obtained by simulation matches the measured value. The value $L = 2.5l$, adopted in all scalar-mixing-layer computations reported here, yields the $c'(y)$ profile that is shown, alongside the measured profile, in figure 1. It is reasonable that L determined in this manner is larger than l because L is the size of the largest possible eddy in the simulation, while l is the size of a 'typical' large eddy in the flow. The ratio L/l is not considered to be a universal constant because the operational definitions of l in different flows are not always equivalent. A markedly different value of the ratio is obtained for the flow considered in §4.1.

The measured profiles of c', and of mixture-fraction skewness and kurtosis shown in figures 2 and 3, exhibit off-centreline local extrema not seen in previous measurements. These features presumably reflect the complicating factors, mentioned earlier, that are not represented in the simulation. Apart from the lack of these features, the simulation is seen to yield mixture-fraction statistics in good overall agreement with measurements. (The vertical differences between pairs of simulation points reflect statistical variability due to the finite number of simulated realizations. As in laboratory flows, individual realizations are asymmetric although ensemble-average profiles of even and odd moments are symmetric and anti-symmetric, respectively.)

Results for the reacting species are presented in figures 4–8. In those figures, symbols denote finite-Da results. In figures 4–7, curves (solid and dashed, respectively) denote results for the limiting cases $Da = \infty$ (fast chemistry) and $Da = 0$ (frozen flow). Results for the limiting cases are based on expressions given by Bilger *et al.* (1991) that relate the fluctuation statistics in those limits to mixture-fraction statistics.

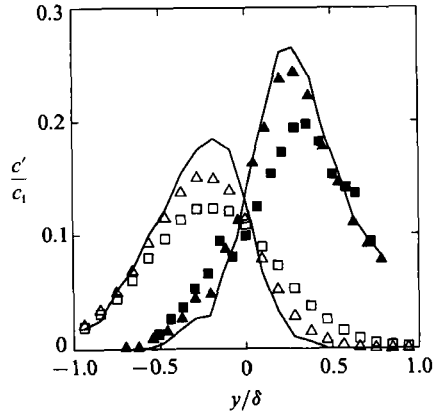

FIGURE 5. Transverse profiles of r.m.s. fluctuation c' of reactant concentration, scaled by inlet concentration c_1, in the scalar mixing layer at $x/M = 21$ for $Da = 0.3$ (□), 1.8 (△), and ∞ (——). Notation as in figure 4. For both species, the frozen-flow limit $Da = 0$ corresponds to the mixture-fraction fluctuation profiles plotted in figure 1.

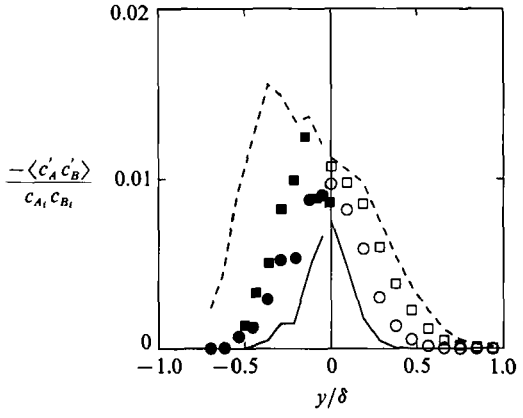

FIGURE 6. Covariance $\langle c'_A c'_B \rangle$ of reacting species, labelled A and B, scaled by inlet concentrations c_{A_1} and c_{B_1}, in the scalar mixing layer at $x/M = 21$ for $Da = 0.3$ (□), 1.8 (○), ∞ (——), and 0 (– – –). Left of centreline: measurements (Bilger *et al.* 1991); right of centreline: simulations.

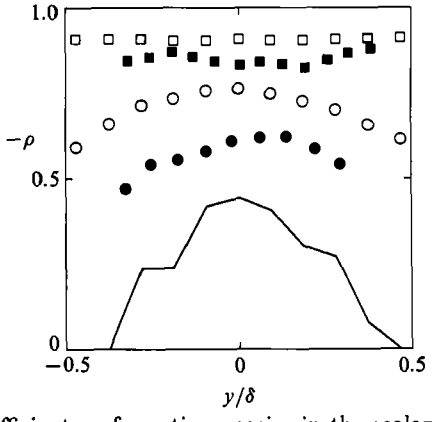

FIGURE 7. Correlation coefficient ρ of reacting species in the scalar mixing layer at $x/M = 21$ for $Da = 0.3$ (□), 1.8 (○), and ∞ (——). Filled symbols: measurements (Bilger *et al.* 1989); open symbols and curve: simulations. (For the case $Da = 0$, ρ is identically equal to −1.)

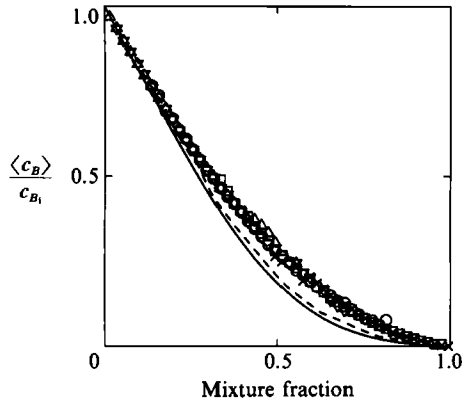

FIGURE 8. Scaled mean concentration $\langle c_B \rangle / c_{B_1}$ of O_3, conditioned on mixture fraction, in the scalar mixing layer at $x/M = 21$. All results are for $Da = 0.3$. Simulations: $y/\delta = -0.4(\triangle), -0.2(\triangledown), 0(\bigcirc), 0.2(\square), 0.4(\times)$. ---, Measurements (Bilger *et al.* 1989); ——, computed lower bound based on instant mixing to the indicated mixture fraction followed by chemical reaction for a time interval x/U.

In figures 4 and 5, measured profiles are shown for NO and simulated profiles are shown for O_3. Since the inlet species have nearly equal diffusivities and inlet concentrations for the cases considered, measured statistics of NO at given y match those of O_3 at $-y$ to within experimental precision. The same holds for computed statistics. Thus, agreement between computations and measurements is indicated if corresponding profiles are mirror images with respect to the transformation $y \rightarrow -y$.

It is evident in figure 4 that computed mean concentrations for finite Da exceed measured values, especially near the centreline. This difference between computed and measured concentrations is to be expected because decaying turbulence is here being modelled as stationary turbulence. Recall that D_T and L are held constant, neglecting observed streamwise variation, particularly the decay of D_T. The method for determining the model parameter D_T gives a result that is smaller than the true value near the grid but larger than the true value farther downstream. The net impact is that species are mixed sooner in the real flow than in the simulation, so the true extent of reaction is greater than the computed result at $x/M = 21$.

In the frozen-flow limit, the model reproduces (to within computational precision) the error-function profile corresponding to a diffusion process with diffusivity D_T acting on the initial profile for a time x/U. This reflects the fact that the random sequence of rearrangement events induces a diffusion process, as mentioned in §2 and demonstrated previously (Kerstein 1991*b*). (Molecular transport may modify the effective diffusivity, Saffman 1960, but the effect is not statistically significant at Pe values of interest here.)

The difference between computed and measured r.m.s. concentration profiles in figure 5 can be attributed to the approximate representation of convective stirring in the model. The model appears to capture the principal qualitative trends and to give quantitative results within 40% of measured values.

The scaled concentration covariance of species A and B is shown in figure 6. Because of the aforementioned reflection symmetry, this quantity is an even function of y, so measured results for $y < 0$ and computed results for $y > 0$ are plotted. The measurements exhibit off-centreline peaks for the two lowest Da values. This feature is not reproduced by the computations.

An alternative normalization of the covariance yields the correlation coefficient

$$\rho = \langle c'_A c'_B \rangle / (c'_A c'_B), \tag{3}$$

plotted in figure 7. (The term $\langle c'_A c'_B \rangle$ denotes the covariance of c_A and c_B, but the quantities c'_A and c'_B, not enclosed in angle brackets, denote the r.m.s. fluctuation of the respective species concentrations.) For the frozen-flow limit of two-stream mixing, $\rho = -1$. Figures 6 and 7 both indicate monotonic dependence on *Da*. Monotonic dependence is not, however, a mathematical requirement. In §4, computed results predicting non-monotonic dependence on *Da* in a three-stream mixing configuration are presented.

It appears that the model performs better with respect to species correlation statistics (figures 6 and 7) than with respect to fluctuation statistics of individual species (figure 5). A comparable outcome is obtained in §4 for a different configuration involving multistream mixing of non-reacting scalars. These results may reflect the mechanistically sound representation of molecular processes in the model. Species correlation statistics reflect intermixing, which is necessarily mediated by molecular diffusion. In contrast, fluctuations of individual species concentrations are induced by convective stirring, with molecular diffusion serving to dissipate fluctuations. Whatever the underlying explanation, it is noteworthy that the correlation statistics, which are directly related to chemical reaction rates, can be predicted with relatively good accuracy.

In figure 8, the scaled mean concentration of O_3, conditioned on mixture fraction, is plotted for five transverse locations. Computed results indicate that the conditioned mean is insensitive to transverse location, in accordance with the measurements of Bilger, Krishnamoorthy & Saetran (1989). Since their measurements at the same set of transverse locations collapse to a single curve, their data are plotted as a curve in figure 8. Also shown is the curve corresponding to instant mixing at $x = 0$ to the indicated mixture fraction, a lower bound on the finite-rate-mixing cases.

Bilger *et al.* (1989) note that the collapse of the conditioned mean may be a useful property for modelling purposes because the transverse variation of species concentrations can be subsumed into a dependence on mixture fraction. This collapse is to be expected because fluid elements undergo large transverse displacements on a timescale shorter than the timescale for chemical reaction. Thus, conditional averages of reactant concentration at various y-locations for given mixture fraction are, in effect, based on the same population of fluid elements.

A surprising aspect of the measured curve is its proximity to the lower bound. In fact, the measured joint p.d.f. of species A and B is found to extend below the corresponding lower bound for that quantity (Bilger *et al.* 1991), suggesting that the conditional p.d.f. of c_B would extend below the bound in figure 8. A possible explanation is that the experimental configuration is not strictly a plug flow; namely, some fluid parcels at given x may have been residing in the flow for a time longer than x/U. Since the model is based on plug flow, it excludes this possibility and gives joint and conditional p.d.f.'s (not shown) that do not extend below the corresponding bounds.

Summarizing the foregoing comparisons, it is found that the model captures the principal trends and features exhibited by species concentration statistics in the reacting-scalar mixing layer. Some differences that have been noted may be attributable to near-field influences, such as the effect of the splitter plate, not reflected in the model. Despite such complications, the measurements provide a useful basis for assessing *Da* effects.

With regard to conserved-scalar mixing, the experimental configuration considered next is advantageous in that the scalar is introduced in a minimally intrusive manner well downstream of the grid, thereby avoiding near-field influences, and the inlet profile allows the development of a richer mixing phenomenology.

4. Mixing downstream of continuous line sources

4.1. *A single line source*

The first application of the linear-eddy modelling concept was to the development of the concentration field downstream of a continuous line source in homogeneous turbulence (Kerstein 1988). Here, the formulation outlined in §2 is applied to single-line-source and two-line-source configurations. Computed results for both configurations are compared to the measurements of Warhaft (1984). Pertinent characteristics of the experiment are shown in table 1. Adopting Warhaft's notation, the source(s) are in a transverse plane a distance x_0 downstream of a turbulence-generating grid. In the terminology of §2, the plane containing the source(s) is the inlet. Streamwise and transverse coordinates referenced to a source are denoted x' and y', respectively. All single-source statistics are even functions of y', so all measured and computed transverse profiles are plotted on the half-line $y' > 0$. For the two-source configuration, the sources are parallel, separated by a distance d, and the transverse coordinate y is referenced to the line midway between the sources. For this configuration, transverse profiles are plotted on the half-line $y > 0$.

As in the mixing-layer application, homogeneous, stationary turbulence is assumed in the simulations, but now, one aspect of flow-field development is incorporated. Simulations corresponding to configurations with two different values of x_0 are performed. In each case, the turbulence integral scale is based on measured flow-field properties at the corresponding value of x_0.

There is an empirical basis for this approach. With regard to the evaluation of D_T, Sirivat & Warhaft (1983) measured the streamwise profile of D_T in the same apparatus used in Warhaft's (1984) line-source measurements, but with a uniform transverse scalar gradient introduced in the inlet plane (their 'toaster' configuration). They observed only a mild (roughly 20%) variation of D_T over the streamwise range considered here, so a representative value $D_T = 8\ \mathrm{cm^2/s}$ is adopted. For application to the line-source measurements, it should be noted that D_T was measured in a flow with mean velocity $U = 630$ cm/s, while the flow velocity for the line-source study was $U = 700$ cm/s. The measured D_T value is therefore multiplied by 700/630, reflecting an assumed proportionality to U. (Roughly the same factor is obtained if proportionality to the measured r.m.s. velocity fluctuation u is assumed). Thus, D_T is assigned the value $8.89\ \mathrm{cm^2/s}$ in the simulations, giving $Pe = 44.4$ (based on $D_M = 0.2\ \mathrm{cm^2/s}$).

This value of Pe indicates that the flow does not correspond to turbulent mixing with a fully developed inertial–convective spectral subrange. Nevertheless, the formulation of §2, based on fully developed inertial-range turbulence, is used for data comparisons. The impact of these considerations on a mechanistic interpretation of the results is discussed in §4.2.

The measured turbulence integral scale l is a more rapidly varying function of x than is D_T. Nevertheless, Warhaft (1984) found that measured x-dependences of transverse profile widths and of species correlation coefficients for configurations with different x_0 exhibit excellent collapse if the transverse coordinate is scaled by $l(x_0)$ in each instance. Thus, mixing statistics within the streamwise range of the

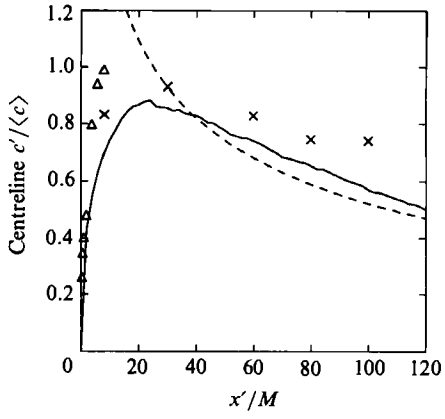

FIGURE 9. Centreline ($y' = 0$) fluctuation intensity $c'/\langle c \rangle$ downstream of a single line source. x' is distance from the source; M is the mesh spacing of the turbulence-generating grid. Measurements (Warhaft 1984) correspond to wires of diameter 0.025 mm (△) and 0.127 mm (×) located at $x_0/M = 52$ relative to the grid. ——, Linear-eddy model; – – –, flapping model.

measurements are consistent with the assumption that flow-field parameters for each case are fixed at inlet-plane values. On this basis, the model parameter L is held constant in each simulation, with a value proportional to the measured integral scale $l(x_0)$. The constant of proportionality is adjusted to obtain the best fit of the simulated centreline ($y' = 0$) fluctuation-intensity profile $c'(x')/\langle c(x') \rangle$ to measurements.

The simulated curve giving the best fit, corresponding to $L = 5.6l$, is compared in figure 9 to measurements downstream of a line source at $x_0/M = 52$. In the experiment, the scalar was introduced by means of a heated wire. Results based on two different wire diameters are shown. Results based on the smaller wire are more representative of the ideal line source, not only because flow disturbance is reduced, but also because concentration statistics are sensitive to the transverse span of the scalar source (Sawford & Hunt 1986; Thomson 1990). In the simulations, the scalar source was introduced in a single cell of the computational domain. For some of the near-field statistics discussed shortly, spatial resolution considerably finer than the Kolmogorov scale L_K was required in the simulations in order to obtain results corresponding to the ideal line source (as indicated by insensitivity of computed results to further increase of resolution).

Also shown in figure 9 is a computed curve based on the 'flapping model' presented in the Appendix, so named because it is based solely on random, rigid displacements of the entire concentration field, omitting any mixing effects *per se*. To the extent that this simple model accounts for experimental or computational results, those results may be viewed as manifestations of large-scale motions rather than the mixing process. In a previous application of the flapping model to the scalar mixing layer, the model was found to agree remarkably well with measured scalar fluctuation statistics (Kerstein 1991*c*).

The flapping model involves one adjustable parameter, the r.m.s. displacement m, which is adjusted to fit the linear-eddy fluctuation-intensity profile in the far field. (As indicated in figure 9 and discussed in the Appendix, the flapping model fails in the near field, giving diverging rather than vanishing fluctuation intensity.) For this purpose, the linear-eddy simulations are implemented over a streamwise interval far exceeding the domain of the measurements. Figure 10 shows the far-field best fit to

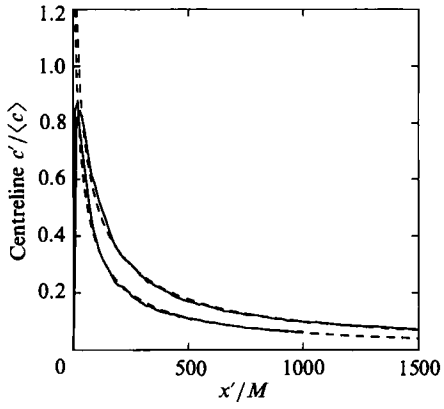

FIGURE 10. Centreline fluctuation intensity downstream of a single line source. ——, Linear-eddy model; ---, flapping model. Upper and lower pairs of curves correspond to line-source locations $x_0/M = 52$ and 20, respectively.

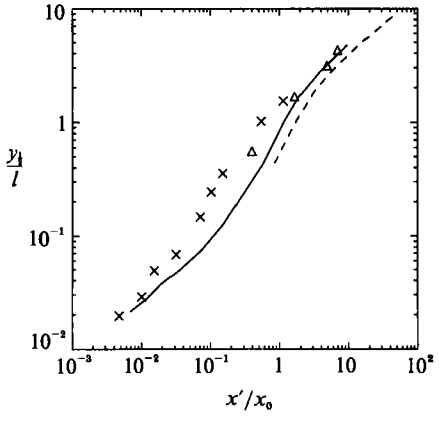

Figure 11. Half-width $y_{\frac{1}{2}}$ of the transverse profile of mean concentration, normalized by the integral scale l measured at x_0/M. Measurements (Warhaft 1984): $x_0/M = 52$ (×), 20 (△). Linear-eddy simulations: $x_0/M = 52$ (——), 20 (---).

linear-eddy simulations for the case $x_0/M = 52$. This fit gives $m = 2.4l$. (The flapping model is fit to the linear-eddy model rather than to the experimental data in order to provide a consistent basis for comparison of the two models.) Figure 10 also shows results for both models for the case $x_0/M = 20$ with the fitted coefficients of proportionality unchanged. These comparisons indicate that the flapping model provides an excellent quantitative characterization of the linear-eddy far-field fluctuation intensity.

The half-width $y_{\frac{1}{2}}(x')$, defined as the y'-location at which the mean concentration is half its centreline value, provides a gross characterization of the growth of the plume downstream of the scalar source. Figure 11 indicates that the simulated streamwise development captures the sigmoidal trend of the experimental data, but that the inflexion point occurs a factor of three too far downstream. The mechanistic basis of the sigmoid was discussed in an earlier modelling study of this configuration (Kerstein 1988). This feature is a manifestation of transitions between three plume-growth regimes, characterized by the elapsed time from origination at the source: (i)

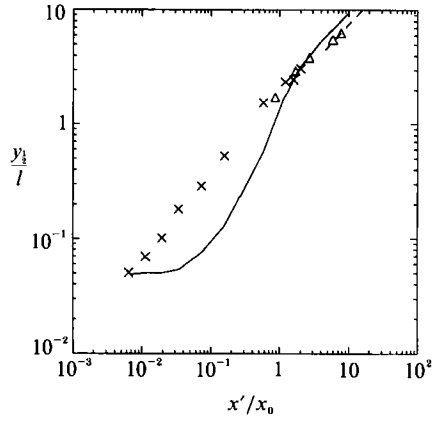

FIGURE 12. Half-width $y_{\frac{1}{2}}$ of the transverse profile of r.m.s. concentration fluctuation, normalized by the integral scale l measured at x_0/M. Measurements (Warhaft 1984): $x_0/M = 52$ (×), 20 (△). Linear-eddy simulations: $x_0/M = 52$ (——), 20 (---).

molecular-diffusive growth during an elapsed time of the order of the Kolmogorov time $t_K = L_K^2/\nu$, (ii) convective growth from t_K until a time of order $t_L = L^2/D_T$ (the 'large-eddy turnover time'), and (iii) turbulent-diffusive growth thereafter. In regimes (i) and (iii), diffusive growth of the form $y_{\frac{1}{2}} \sim x'^{\frac{1}{2}}$ is obtained, with diffusion coefficients D_M and D_T, respectively. In regime (ii), the size of the eddy whose turnover time equals the elapsed time $t = x'/U$ is of order $(t/t_K)^{\frac{3}{2}}L_K$, based on inertial-range scaling (Tennekes & Lumley 1972). In the model, the typical size of the largest mapping segment affecting the plume in this regime is likewise of this order. Because eddies are represented by instantaneous mapping events in the model, this size determines the typical plume width in regime (ii), yielding $t^{\frac{3}{2}}$ scaling (Kerstein 1991*b*). In contrast, real eddies are continuous processes in time, so throughout regime (ii) the plume undergoes a transverse convective displacement of order vt. (v is the transverse r.m.s. velocity fluctuation, here interpreted as the typical transverse velocity of a large eddy.) This displacement is the dominant plume growth mechanism in regime (ii), yielding the classical linear growth in this regime.

This analysis indicates that the instantaneous nature of mapping events in the model impacts the representation of the early development of the mixing field, during which the finite time duration of eddies plays an influential role. This artifact of the model, analysed elsewhere in more detail (Kerstein 1991*b*), is clearly evident in data comparisons involving transverse profiles of r.m.s. concentration fluctuation. Figure 12 shows measured and simulated half-widths of those profiles. The cause of the underprediction of profile width in the intermediate regime is evident from examination of the profiles plotted in figures 13 and 14.

The simulated profiles in the near field are characterized by steep shoulders transitioning to broad tails. These features reflect the dichotomy between the profile width for a typical realization (as characterized by the half-width) and the width based on the second moment of the profile with respect to y'. As the broad tails suggest, the second-moment width greatly exceeds the half-width. The width based on the second moment is of order $(D_T t)^{\frac{1}{2}}$ for all $t > t_K$ because the random sequence of mapping events constitutes a diffusion process on the transverse line with diffusion coefficient D_T (Kerstein, 1991*b*).

The cause of this artifact is again the instantaneous nature of mapping events. The relatively infrequent occurrence of events of segment size much greater than

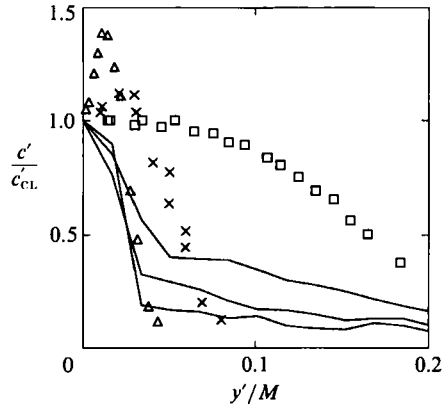

FIGURE 13. Transverse profiles of r.m.s. concentration fluctuation c', normalized by centreline values, for $x_0/M = 52$. y' is transverse distance from the source. Measurements (Warhaft 1984): $x'/M = 0.36$ (△), 1.0 (×), 3.8 (□). Curves are linear-eddy simulation results for the same x'/M values. (Height of the tails increases with increasing x'.)

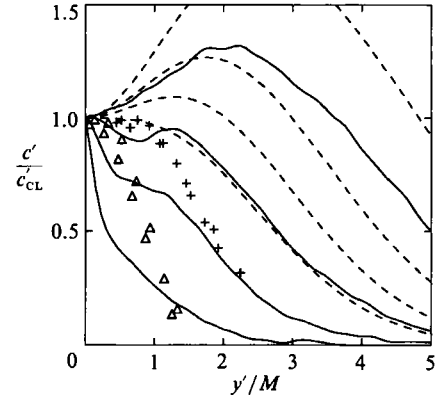

FIGURE 14. Transverse profiles of r.m.s. concentration fluctuation c', normalized by centreline values, for $x_0/M = 52$. Measurements (Warhaft 1984): $x'/M = 30$ (△), 100 (+). Solid and dashed curves are linear-eddy and flapping-model results, respectively, for $x'/M = 30$, 100, 200, and 500. (Height of the curves increases with increasing x'.)

$(t/t_K)^{\frac{3}{2}} L_K$ during an elapsed time t is the dominant mechanism determining the second-moment width, but does not contribute to the half-width. In real flows with eddies of finite time duration, this dichotomy is absent.

Figure 14 indicates an eventual transition from this behaviour to the emergence of an off-centreline peak of the r.m.s. fluctuation profile. Figure 15, showing far-field measured and simulated profiles for a different value of x_0/M, indicates improved performance of the model in the far field, with the off-centreline peak developing roughly conforming to measurements. The flapping-model profiles shown in figures 14 and 15 indicate that the far-field qualitative behaviour can be interpreted simply as a manifestation of flapping. An interpretation has also been proposed based on stretching and eventual molecular blending of lamellae near the centreline containing relatively high concentration gradients (Kerstein 1988).

Flapping-model profiles are omitted from figure 13 because they are essentially horizontal on the scale of that plot. The widths of these profiles are much larger than

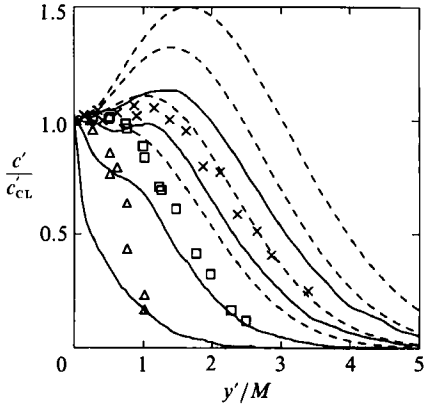

FIGURE 15. Transverse profiles of r.m.s. concentration fluctuation c', normalized by centreline values, for $x_0/M = 20$. Measurements (Warhaft 1984): $x'/M = 17$ (△), 63 (□), 133 (×). Solid and dashed curves are linear-eddy and flapping-model results, respectively, for $x'/M = 17$, 63, 133, and 200. (Height of the curves increases with increasing x'.)

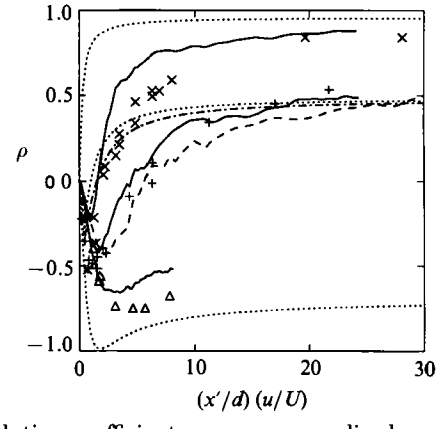

FIGURE 16. Species correlation coefficient ρ versus normalized coordinate $(x'/d)\,(u/U)$, where d is the separation of the two line sources, U is the mean flow velocity, and u is the streamwise r.m.s. velocity fluctuation. Measurements (Warhaft 1984): $d/l = 0.5$ (×), 2 (+), 8 (△). Solid and dotted curves are linear-eddy and flapping-model results, respectively, for the corresponding d/l values, for $x_0/M = 52$. Dashed and chain-dashed curves are linear-eddy and flapping-model results, respectively, for $d/l = 2$, $x_0/M = 20$.

measured values, reflecting the aforementioned failure of the flapping model in the near field.

Finally, it is noted that simulation results shown in figures 11 and 12 for different values of x_0/M do not collapse as precisely as measured quantities on the scaled plots. Since the mechanistic basis of the collapse of the experimental results is unclear, no interpretation is attempted except to note that the sensitivity to x_0/M does not have a great impact on the predictive capability of the model.

4.2. *Interference of two line sources*

For the experimental configuration consisting of two parallel heated wires separated by a distance d, both a distance x_0 downstream of the grid, Warhaft (1984) performed the thermal analogue of the following measurement. Suppose that the wires are

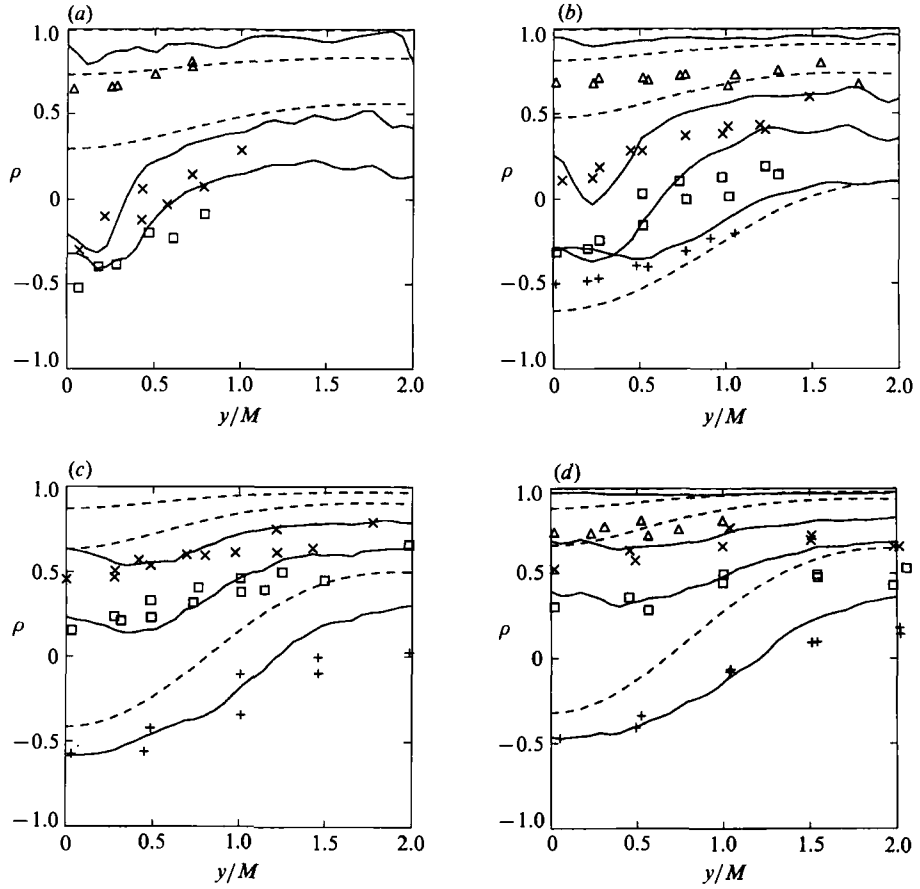

FIGURE 17. Transverse profiles of species correlation coefficient ρ for $x_0/M = 20$. y is transverse distance referenced to the line midway between the two sources. Measurements (Warhaft 1984): $d = 1.2$ mm (△), 8 mm (×), 14 mm (□), 35 mm (+). Solid and dashed curves are linear-eddy and flapping-model results, respectively, for the corresponding d-values. (*a–d*): $x'/M = 17, 33, 93, 133$.

equal-intensity sources of distinct, equal-diffusivity species A and B, respectively. By combining results for the one-wire and two-wire configuration, Warhaft obtained the correlation coefficient ρ, given by (3), at various downstream locations x' and transverse locations y relative to the line midway between the wires.

Measurements were reported for values of x_0/M ranging from 5 to 60 and for $d/l(x_0)$ ranging from 0.075 to 10. For given $d/l(x_0)$, measured centreline ($y = 0$) streamwise profiles of ρ exhibit excellent collapse over the range of x_0/M values when plotted with respect to the 'normalized convective time' $[x'/d][u(x_0)/U]$, where $u(x_0)$ is the streamwise r.m.s. velocity fluctuation measured at x_0. Therefore, the experimental results plotted in figure 16 include data reported for all x_0/M values, not just the values 20 and 52 for which simulations are performed. (Simulation results exhibit some sensitivity to x_0/M, but not so large as to have an impact on the data comparisons.) Three representative values of $d/l(x_0)$ are selected for data comparison in figure 16. Measured and simulated transverse profiles of ρ for other values of $d/l(x_0)$ are shown in figure 17.

The overall agreement of simulated results with measurements is good, roughly comparable to the performance of the particle-pair dispersion model applied to this

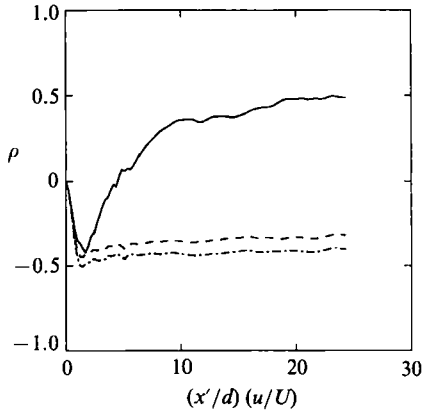

FIGURE 18. Species correlation coefficient ρ versus normalized coordinate $(x'/d)\ (u/U)$, based on linear-eddy simulation, for $x_0/M = 52$, $Da = 0$ (solid), 2.7 (chain-dashed), ∞ (dashed).

configuration by Thomson (1990). Remarkably, the flapping model reproduces the principal qualitative trends. In figure 16, it reproduces the dependence of the far-field asymptotc, the rate of convergence to the asymptote, and the minimum value of ρ on $d/l(x_0)$. In figure 17, it reproduces the dependence of the transverse width of the profiles on $d/l(x_0)$ and on x'/M.

Thus, one is not compelled to invoke mixing mechanisms to interpret the trends, though the correlation coefficient is presumably sensitive to the mixing process. The quantitative as well as qualitative agreement of both the linear-eddy model and the particle-pair dispersion model with the measurements is, ostensibly, evidence of that sensitivity. However, both models are based on high-Re phenomenology whose applicability to this moderate-Re flow is problematic. It is remarkable that these mixing models nevertheless yield accurate predictions for this configuration. This result is consistent with the observation in §3 that the correlation statistics of reacting species are well characterized by the linear-eddy model.

4.3. *Multi-stream mixing with finite-rate chemistry*

The foregoing results do not assure that either the particle-pair dispersion model or the linear-eddy model adequately characterizes all aspects of the two-line-source configuration. In particular, recognizing that the experiment was partly motivated by its implications for turbulent reacting flows, it is of interest to consider how ρ is affected by a finite-rate chemical reaction between species A and B. This three-stream mixing problem (the streams being the two sources and the inert background) has the potential to exhibit qualitatively different Da dependences than two-stream mixing problems such as the scalar mixing layer. This possibility is indicated by the fact that the spatial dependence of ρ in the frozen-flow limit considered in §4.2 exhibits a rich phenomenology, in contrast to the mathematical requirement $\rho = -1$ for two-stream mixing of non-reacting species.

Simulated results for cases involving chemical reaction as well as frozen flow are shown in figures 18 and 19. Inlet conditions and flow parameters correspond to the case $x_0/M = 52$, $d/l(x_0) = 2$. Thus, the frozen-flow streamwise profile plotted in figure 18 is the same as the profile of figure 16 for this case. Chemical reaction is introduced by incorporating the bimolecular reaction-rate expression, (2), into (1) governing molecular effects. A suitable definition of Da for this configuration is $Da = k(c_{A_1}+c_{B_1})\ \Delta/U$, where the assumed inlet condition is a uniform concentration

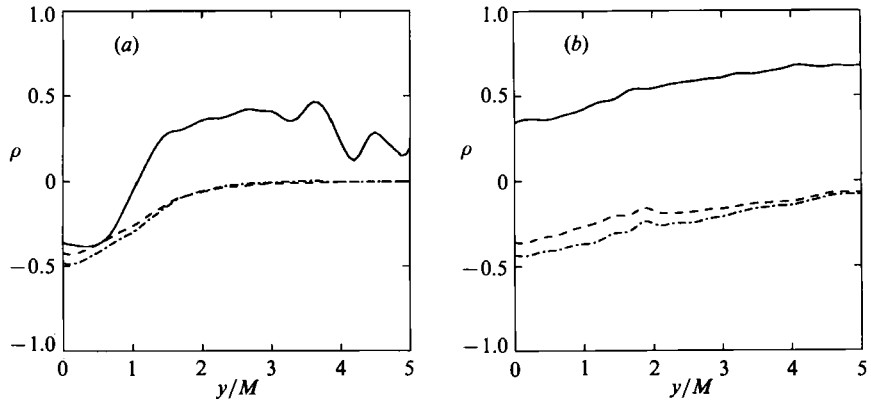

FIGURE 19. Transverse profiles of species correlation coefficient ρ, based on linear-eddy simulation, for $x_0/M = 52$, $Da = 0$ (solid), 2.7 (chain-dashed), ∞ (dashed). (a, b): $x'/M = 100$, 500.

c_{A_i} of species A over the interval $\frac{1}{2}(d-\Delta) < y < \frac{1}{2}(d+\Delta)$ and a uniform concentration c_{B_i} of species B over the interval $\frac{1}{2}(-d-\Delta) < y < \frac{1}{2}(-d+\Delta)$. The two inlet concentrations are taken to be equal, with their common value denoted c_i. Ideal line sources correspond to the limit $\Delta \to 0$ with the product $c_i\Delta$, determining the inlet species fluxes, held fixed. As in §4.2, Δ is chosen to be the width of a single cell of the discretized computational domain, with resolution sufficient to eliminate finite-source-size effects. Since (1) and (2) governing molecular processes are linear with respect to each reactant, the simulated evolution depends only on the product $kc_i\,\Delta$ in the ideal-line-source limit, so only Da need be specified. (More general, nonlinear forms of the molecular governing equations would involve additional dependence on c_i. In that situation, a suitable choice of k might be the value corresponding to the NO–O_3 reaction, with $c_i\,\Delta$ then determining Da.) Simulated results for $Da = 2.7$ and ∞ are compared in figures 18 and 19 to the frozen-flow case.

An interesting feature of the results is the occurrence of non-monotonic dependence of ρ on Da. Though mathematically possible for two-stream as well as multi-stream mixing, this feature is not found in the experimental or computational results for the two-stream configuration examined in §3.

Other features apparent in figure 19 indicate the sensitivity of Da effects to aspects of the mixing process. In frozen flow, ρ is positive at large y because species that are intermixed near the centreline remain intermixed as they are transported far from the centreline. The flow at large y can be characterized as intermixed patches dispersed in a background devoid of either species, giving a correlation coefficient that converges to a positive constant as the volume fraction of the intermixed patches vanishes. With chemical reaction, however, the deficient reactant in each intermixed patch is eventually depleted, leading to small patches containing one or the other reactant. This gives a negative correlation coefficient. Furthermore, if the volume fraction of these patches is of order of $\epsilon \ll 1$, then it follows from the definition of ρ that ρ is of order $-\epsilon$. Hence the vanishing of ρ for large y in the chemically reacting cases.

This scenario also implies that, at given y far from the centreline, ρ should be more negative with increasing Da. The computed curves of figure 19(a) for $Da = 2.7$ and ∞ do in fact cross over at large y and the fast-chemistry curve becomes more negative. The magnitude of the effect, though small, is statistically significant because the simulated flow fields are identical in the two cases. (The y-span of the

computational domain is not sufficient to demonstrate the large-y crossover of the profiles of figure 19(b), corresponding to a transverse plane farther downstream, but the trend suggests an eventual crossover.) Thus, ρ becomes monotonic in Da where the underlying mixing mechanism requires this result, but is non-monotonic in the region where the greater complexity of the mixing process allows non-monotonicity.

These predictions indicate that measurements of Da effects in multi-stream mixing configurations would be valuable because qualitative trends as well as quantitative results may be sensitive to mixing effects not reflected in frozen-flow statistics.

5. Discussion

The results presented here, in conjunction with previous results (Kerstein 1991a, b), serve to identify those aspects of the turbulent mixing process that can be adequately represented by a one-dimensional formulation involving discrete, instantaneous fluid motions rather than continuous flow. The general inference is that properties sensitive to the cumulative effects of many eddies are well represented. Properties sensitive to the predominant influence of a single eddy may be inadequately represented if the time development of that eddy is neglected. This point is emphasized in the discussion of the near-field transverse development of the plume downstream of a continuous line source, which is influenced primarily by the largest eddy convecting the mixing field.

Apart from this caveat, linear-eddy model results are in overall quantitative agreement with the fluctuation statistics of conserved scalars for the configurations examined, and in qualitative agreement with statistics of reacting scalars. With regard to conserved-scalar mixing, the flapping model applied here to continuous-line-source configurations and elsewhere (Kerstein 1991c) to the scalar mixing layer indicates that the principal features of the measurements can be interpreted without invoking a mixing process *per se*. This does not imply that the enhancement of mixing by fluid motions is unimportant in these configurations, but rather that the statistical quantities being examined may not be the principal indicators of such effects.

In that regard, the sensitivity of chemical-kinetic effects to the mixing process has been highlighted. First, it was shown that the quantitative accuracy of the linear-eddy model with regard to conserved-scalar statistics does not generalize to commensurate accuracy with regard to reacting scalars (though qualitative features are still captured). Second, simulation of chemical-kinetic effects in a multi-stream mixing configuration yielded predictions whose interpretation is based on detailed consideration of mixing mechanisms. Analogous measurements, possibly performed by suitable modification of the inlet concentration profile in the apparatus of Bilger *et al.* (1991), would be useful in this regard. Even so simple a variation of that experiment as the introduction of unequal reactant concentrations might be interesting, since it would break the symmetry between the reactants.

Further insight into mixing mechanisms may be provided by measurements in which Re and Sc as well as Da are varied for a given inlet concentration profile. In particular, the selection of reactants with much different molecular diffusivities would introduce differential molecular diffusion effects, of practical importance in many applications but difficult to incorporate in conventional modelling approaches. All these aspects are addressed by the linear-eddy model (Kerstein 1989, 1990).

Additional measurements may also aid in interpreting the observation that the linear-eddy model yields more accurate predictions of species correlation statistics

than of concentration fluctuations of individual species, both in non-reacting and reacting cases. If this is a robust feature, a model may prove to be a reliable predictor of reaction rates in turbulent flows.

Apart from the question of model validation, the data comparisons presented here indicate that a systematic correspondence can be established between the salient features of species concentration statistics measured in various turbulent plug flows and the inlet concentration profiles and chemical reaction mechanisms in those flows. Turbulent-reacting-flow modelling based on a reduced description of the flow field can succeed only to the extent that species evolution is governed by the inlet concentration profiles, reaction mechanisms, and gross features of the flow rather than depending on configuration-specific details of the flow field.

The author would like to thank R. W. Bilger, G. Kosály and Z. Warhaft for helpful discussions. This research was supported by the Division of Chemical Sciences, Office of Basic Energy Sciences, US Department of Energy.

Appendix. Flapping model of scalar fluctuation statistics

In a companion paper (Kerstein 1991*c*), a flapping model motivated by Gifford's (1959) fluctuating plume model is formulated for turbulent mixing fields with planar symmetry, and predictions are compared to fluctuation statistics measured in scalar mixing layers. Here, the model is applied to the single-line-source and two-line-source configurations considered in §4.

Single-point scalar fluctuation statistics in a transverse plane at given x' are assumed to reflect the flapping of a scalar concentration profile of fixed functional form $\chi(y)$. In the case of two line sources emitting species A and B respectively, two profiles $\chi_A(y)$ and $\chi_B(y)$ are specified. Flapping, i.e. rigid displacement of the entire concentration field, is assumed to induce a Gaussian distribution of displacements $\hat{y}$ of that field. The distribution of $\hat{y}$ is assumed to have zero mean, and its standard deviation m is treated as an adjustable parameter.

For each source, the fixed profile is assumed to be Gaussian with zero mean and standard deviation $\sigma = (2D_{\mathrm{T}}t)^{\frac{1}{2}}$, where $t = x'/U$ is the elapsed time for plume growth. (The Gaussian assumption implies that the integral of the profile over y has been normalized to unity, an assumption that is convenient but not essential.) This profile may be regarded as a gross characterization of the concentration field at x' referenced to its instantaneous centroid. The assumed expression for σ is based on a turbulent diffusivity picture valid only in the far field, hence the failure of the model in the near field, noted in §4.1. (The underlying mechanism is in fact better justified in the near-field convective regime of plume growth than in the far-field turbulent-diffusive regime. The present formulation addresses the latter regime for purposes of comparison to linear-eddy results.) As in linear-eddy simulations, the value of D_{T} is assigned based on flow-field conditions at the source, omitting any variation farther downstream.

The deviation of the instantaneous centroid from its mean location is characterized by the random displacement $\hat{y}$. It is assumed, somewhat arbitrarily, that the r.m.s. displacement m is independent of x', with plume growth effects subsumed in the x'-dependence of σ. This arbitrariness reflects the artificiality of the underlying mechanistic picture, relying solely on rigid displacements to generate concentration fluctuations.

Based on these assumptions, the nth moment of concentration at a given location

(x', y') relative to a given source is obtained by integrating $\chi^n(y'-\hat{y})$ over the p.d.f. of displacements $\hat{y}$. Thus,

$$\langle c^n(x', y')\rangle = \frac{1}{(2\pi)^{(1+n)/2}\sigma^n m}\int_{-\infty}^{\infty} d\hat{y}\exp\left[-\frac{\hat{y}^2}{2m^2}-\frac{n(y'-\hat{y})^2}{2\sigma^2}\right]. \tag{A 1}$$

Evaluation of the integral gives

$$\langle c^n(x', y')\rangle = \frac{\exp\left\{-\dfrac{y'^2}{2[\sigma^2/n][1+n(m/\sigma)^2]}\right\}}{[(2\pi)^{\frac{1}{2}}\sigma]^n[1+n(m/\sigma)^2]^{\frac{1}{2}}}, \tag{A 2}$$

where $\sigma = (2D_T x'/U)^{\frac{1}{2}}$. Various quantities of interest are obtained using (A 2), e.g. the r.m.s. fluctuation $c'(x', y') = [\langle c^2(x', y')\rangle - \langle c(x', y')\rangle^2]^{\frac{1}{2}}$ plotted in figures 13–15. The expression

$$c'(x', 0)/\langle c(x', 0)\rangle = \left[\frac{1+(m/\sigma)^2}{[1+2(m/\sigma)^2]^{\frac{1}{2}}}-1\right]^{\frac{1}{2}} \tag{A 3}$$

is obtained for the centreline fluctuation intensity plotted in figures 9 and 10.

Evaluation of the correlation coefficient of A and B in the two-line-source configuration requires, in addition to (A 2), the cross-moment $\langle c_A(x', y)\, c_B(x', y)\rangle$, where y is the transverse coordinate referenced to the line midway between the sources. For source separation d, $\chi_A(y)$ and $\chi_B(y)$ are both assumed to be Gaussian, with standard deviation σ, but with respective means $\frac{1}{2}d$ and $-\frac{1}{2}d$. Integration of the product $\chi_A(y-\hat{y})\,\chi_B(y-\hat{y})$ over the p.d.f. of displacements $\hat{y}$ gives

$$\langle c_A(x', y)\, c_B(x', y)\rangle = \frac{1}{(2\pi)^{\frac{3}{2}}\sigma^2 m}\int_{-\infty}^{\infty} d\hat{y}\exp\left[-\frac{\hat{y}^2}{2m^2}-\frac{(y-\hat{y}+\frac{1}{2}d)^2+(y-\hat{y}-\frac{1}{2}d)^2}{2\sigma^2}\right]. \tag{A 4}$$

Evaluation of the integral gives

$$\langle c_A(x', y)\, c_B(x', y)\rangle = \frac{\exp\left[-\dfrac{(y+\frac{1}{2}d)^2+(y-\frac{1}{2}d)^2+(dm/\sigma)^2}{2(\sigma^2+2m^2)}\right]}{2\pi\sigma^2[1+2(m/\sigma)^2]^{\frac{1}{2}}}. \tag{A 5}$$

The correlation coefficient is expressed in terms of the foregoing results as

$$\rho(x', y) = \frac{\langle c_A(x', y)\, c_B(x', y)\rangle - \langle c(x', y+\frac{1}{2}d)\rangle\langle c(x', y-\frac{1}{2}d)\rangle}{c'(y+\frac{1}{2}d)\, c'(y-\frac{1}{2}d)}. \tag{A 6}$$

This expression is used to compute the flapping-model curves of figures 16 and 17.

Evaluating this expression for $y = 0$ in the limit $x' \to \infty$ (i.e. $\sigma \to \infty$), the flapping-model result for the far-field asymptote of the centreline correlation coefficient is

$$\rho(\infty, 0) = \frac{2m^2-d^2}{2m^2+d^2}. \tag{A 7}$$

Taking $m = 2.4l(x_0)$ based on the fit to the linear-eddy centreline fluctuation intensity (figure 10) for $x_0/M = 52$, this gives $\rho(\infty, 0) = 0.96$, 0.48, and -0.70 for the cases $d/l(x_0) = 0.5$, 2, and 8 respectively. The results of this simple analysis agree surprisingly well with far-field measurements, plotted in figure 16, for the corresponding cases. The mechanistic basis of the good agreement of this and other flapping-model predictions with experimental results is not yet clear.

REFERENCES

BILGER, R. W., KRISHNAMOORTHY, L. V. & SAETRAN, L. R. 1989 Use of conditional averaging to obtain biogeochemical reaction rates and stoichiometries under turbulent mixing. *Proc. Tenth Australasian Fluid Mech. Conf.*, pp. 4.33–4.36.

BILGER, R. W., SAETRAN, L. R. & KRISHNAMOORTHY, L. V. 1991 Reaction in a scalar mixing layer. *J. Fluid Mech.* **233**, 211–242.

GHONIEM, A. F., HEIDARINEJAD, G. & KRISHNAN, A. 1989 Turbulence-combustion interactions in a reacting shear layer. In *Turbulent Reactive Flows* (ed. R. Borghi & S. N. B. Murthy.) Lecture Notes in Engineering, vol. 40, pp. 638–671. Springer.

GIFFORD, F. A. 1959 Statistical properties of a fluctuating plume dispersion model. *Adv. Geophys.* **6**, 117–137.

KERSTEIN, A. R. 1988 A linear-eddy model of turbulent scalar transport and mixing. *Combust. Sci. Technol.* **60**, 391–421.

KERSTEIN, A. R. 1989 Linear-eddy modeling of turbulent transport. II: Application to shear layer mixing. *Combust. Flame* **75**, 397–413.

KERSTEIN, A. R. 1990 Linear-eddy modelling of turbulent transport. Part 3. Mixing and differential molecular diffusion in round jets. *J. Fluid Mech.* **216**, 411–435.

KERSTEIN, A. R. 1991*a* Linear-eddy modeling of turbulent transport. Part V: Geometry of scalar interfaces. *Phys. Fluids* A **3**, 1110–1114.

KERSTEIN, A. R. 1991*b* Linear-eddy modelling of turbulent transport. Part 6. Microstructure of diffusive scalar mixing fields. *J. Fluid Mech.* **231**, 361–394.

KERSTEIN, A. R. 1991*c* Flapping model of scalar mixing in turbulence. *Phys. Fluids* A **3**, 2838–2840.

KERSTEIN, A. R. 1992 Linear-eddy modeling of turbulent transport. Part 4. Structure of diffusion flames. *Combust. Sci. Technol.* **81**, 75.

LARUE, J. C. & LIBBY, P. A. 1981 Thermal mixing layer downstream of a half-heated grid. *Phys. Fluids* **24**, 597–603.

LEONARD, A. 1980 Vortex methods for flow simulation. *J. Comput. Phys.* **37**, 289–335.

LI, K. T. & TOOR, H. L. 1986 Turbulent reactive mixing with a series-parallel reaction: Effect of mixing on yield. *AIChE J.* **32**, 1312–1320.

LIBBY, P. A. 1975 Diffusion of heat downstream of a turbulence grid. *Acta Astronaut.* **2**, 867–878.

MA, B.-K. & WARHAFT, Z. 1986 Some aspects of the thermal mixing layer in grid turbulence. *Phys. Fluids* **29**, 3114–3120.

MAO, K. W. & TOOR, H. L. 1971 Second-order chemical reactions with turbulent mixing. *Indust. Eng. Chem. Fundam.* **10**, 192–197.

SAFFMAN, P. G. 1960 On the effect of molecular diffusivity in turbulent diffusion. *J. Fluid Mech.* **8**, 273–283.

SAWFORD, B. L. & HUNT, J. C. R. 1986 Effects of turbulence structure, molecular diffusion and source size on scalar fluctuations in homogeneous turbulence. *J. Fluid Mech.* **165**, 373–400.

SIRIVAT, A. & WARHAFT, Z. 1983 The effect of a passive cross-stream temperature gradient on the evolution of temperature variance in grid turbulence. *J. Fluid Mech.* **128**, 323–346.

TENNEKES, H. & LUMLEY, J. L. 1972 *A First Course in Turbulence.* MIT Press.

THOMSON, D. J. 1990 A stochastic model for the motion of particle pairs in isotropic high-Reynolds-number turbulence, and its application to the problem of concentration variance. *J. Fluid Mech.* **210**, 113–153.

WARHAFT, Z. 1984 The interference of thermal fields from line sources in grid turbulence. *J. Fluid Mech.* **144**, 363–387.